Controlled synthesis and enhanced luminescence of BiOCl:Eu^{3+} ultrathin nanosheets†

Yangyang Guo,[a] Zhijun Zhang,[a] Gangqiang Zhu,[b] Weibin Zhang[a] and Woochul Yang*[a]

BiOCl:Eu^{3+} ultrathin nanosheets were synthesized through a facile solvothermal method with the assistance of polyvinyl pyrrolidone. The ultrathin nanosheets showed a size ranging from 50–100 nm and a height of 2.9 nm, which is about four [Cl–Bi–O–Bi–Cl] layers. In addition, the luminescence properties and mechanism were investigated in detail, and compared with that of the nanoplate. It was found that the luminescence intensity for the BiOCl:Eu^{3+} ultrathin nanosheet was 6 times stronger than that of the nanoplate. Importantly, the oxygen vacancies act as a luminescence centers, and there was effective energy transfer from BiOCl ultrathin nanosheets to Eu^{3+} ions. In BiOCl:Eu^{3+} ultrathin nanosheets, white-light emission was observed under near-ultraviolet (NUV) excitation. These BiOCl:Eu^{3+} ultrathin nanosheets exhibit great potential as color-emitting phosphors for white light-emitting diode applications.

1. Introduction

Recently, two-dimensional (2D) materials composed of a single or few atomic layers have attracted tremendous interest,[1–4] because of their fascinating potential applications in electronics,[5] catalysis,[6] energy storage,[7] solar cells,[8] wearable devices,[9] and luminescence.[10] 2D materials with nanoscale thicknesses are quite alluring candidates for phosphors because of their large surface-to-volume ratio compared to bulk, which improves the photoelectric performance of the semiconductors.[11,12] Moreover, these materials are suitable for fabricating optoelectronic devices, such as electroluminescence panels, which consist of a stack of functional layers or sheets.[13] Therefore, an emphatic work has been done on fabricating the 2D materials to explore their full potential applications.

Bismuth oxychloride (BiOCl) is an indirect band gap semiconductor of group V–VI–VII family, with a wide band gap of 3.5 eV.[14] In particular, BiOCl presents a tetragonal structure with [Cl–Bi–O–Bi–Cl] layers stacked together via weak van der Waals interaction through the Cl atoms along the c-axis. Also, [Bi$_2$O$_2$]$^{2+}$ layers are sandwiched between two slabs of halogen ions. The layered structure of BiOCl exhibits excellent electronic and optical properties, with many important and potential applications such as phosphor, photocatalyst, gas sensor, magnetic materials, and pigments in the cosmetic industry.[15–20] Furthermore, BiOCl has a relatively low phonon energy (as low

as ~400 cm^{-1}) compared to other inorganic compounds, which improves the probability of radiative transition.[21] The wide band gap of BiOCl can provide an optical window for the inherent quenching of rare earth ions.[22] In addition, the ionic radius and charge of Bi^{3+} are comparable with trivalent rare earth ions Eu^{3+}, which is beneficial for Eu^{3+} replacing Bi^{3+} in the BiOCl host lattice. Therefore, high luminescence quantum efficiency is expected to be obtained in BiOCl:Eu^{3+} phosphors. Li et al. synthesized BiOCl:Eu^{3+} powder, which possessed a broad excitation band in the near-ultraviolet (NUV) region, through a solid-state method. The phosphors exhibited great potential as red-emitting phosphors for white LED, owing to their excellent broadband NUV excitation ability and special far-red emission property.[23] Yu et al. reported the up-conversion emission and cathodoluminescence (CL) of Yb^{3+} ions activated BiOCl:Ho^{3+} phosphors. These phosphors showed excellent CL properties and the CL emission intensity increased with increasing accelerating voltage and filament current.[24] Armita et al. reported the luminescence of nanoflakes/BiOX:Eu^{3+} (X = Cl, Br, I) and suggested that both BiOCl and BiOBr were good host matrices for RE^{3+} ions to exhibit effective luminescence properties as well as excellent photocatalytic properties under sunlight irradiation.[25] In our previous work, the luminescence of nanoflower-like structures showed that Eu^{3+} and Sm^{3+}-activated BiOCl, where flower-like structure exhibited a strong red emission corresponding to the typical f–f transitions of Eu^{3+} and Sm^{3+}, respectively.[26] Xie et al. reported the ultrathin BiOCl nanosheet with excellent catalytic activity related to the presence of oxygen vacancy defects.[27] Zhao et al. carried out systematic calculation of the electronic structure and studied the optical properties of BiOCl:Eu^{3+} using first-principles

^{a}Department of Physics, Dongguk University, Seoul, 04620, Korea. E-mail: wyang@dongguk.edu

^{b}Department of Physics, Shaanxi Normal University, Xi'an, 710062, China

method. He revealed that BiOCl:Eu^{3+} was favorable not only for luminescence but also for photocatalysis applications.[28,29]

However, to the best of our knowledge, only a few studies have been undertaken to probe into the luminescence properties of BiOCl:Eu^{3+} 2D material. Therefore, we synthesized BiOCl:Eu^{3+} nanoplates and ultrathin nanosheets using a facile solvothermal method. The luminescence properties, depending on the thickness and the exposed facets, were investigated in detail. The density of oxygen vacancies in the lattice structure is also substantiated.

2. Experimental section

2.1 Sample preparation

All the chemical reagents used in this work were of analytical grade, and ere applied during the synthesis of BiOCl:Eu^{3+} ultrathin nanosheets, without any further purification. Stoichiometric amounts of Eu(NO$_3$)$_3$, Bi(NO$_3$)$_3 \cdot$5H$_2$O and 0.52 g PVP were dissolved in 32.5 mL mannitol solution (0.1 M) with vigorous stirring for 10 min. Then, 6.5 mL of saturated NaCl solution was slowly added to the above mixture, producing a uniform white suspension. After 30 min of agitation, the mixture was transferred into a Teflon-lined stainless steel autoclave of 50 mL capacity, and the autoclave was then placed in an oven with a temperature of 160 °C for 3 h. Afterward, the autoclave was allowed to naturally cool down to room temperature (RT). The resulting precipitate was collected, and washed for several times with deionized water and ethanol. The obtained powder was dried at 70 °C for 4 h for further characterization. Similarly, the BiOCl:Eu^{3+} nanoplates were synthesized by the same experimental method without the surfactant (PVP).

2.2 Characterization

X-ray diffraction (XRD) data was collected at room temperature by D/Max 2550 diffractometry (Rigaku, Japan) at a scanning rate of 5 degree per min in the 2θ range of 10–80° with Cu Kα1 radiation (λ = 1.54056 Å) at 40 kV and 100 mA. The transmission electron microscopy (TEM) and high-resolution TEM (HRTEM) images of the samples were taken with a JEM-2100 electron microscope (JEOL, Japan) operated at an acceleration voltage of 200 kV. The UV-vis diffuse reflectance spectra were measured by Lambda 950 UV-VIS-NIR spectrophotometry (Perkin-Elmer, USA) in the wavelength range of 300–700 nm. The excitation and emission spectra of the samples were recorded at RT by fluorescence spectrophotometry (F-4600 Hitachi, Japan). The scan speed was fixed at 240 nm min^{-1}, and the photomultiplier tube voltage and slit widths were fixed for all the samples at 700 V and 2.5 nm, respectively.

3. Result and discussion

3.1 Phase formation of BiOCl:Eu^{3+} ultrathin nanosheet and nanoplate

Fig. S1 (ESI†) shows the XRD patterns of the synthesized Bi$_{0.9}$Eu$_{0.1}$OCl ultrathin nanosheet and nanoplate and the standard data of BiOCl (JCPDS card no. 06-0249). All diffraction peaks are

in good agreement with the values in the JCPDS card, indicating that the samples are of single phase, and doping of Eu^{3+} ions does not cause any significant changes to the host material. All the samples were crystallized in tetragonal phase ($a = b = 0.3891$ nm, $c = 0.7369$ nm) with the space group P4/nmm. The XRD patterns of nanoplates and nanosheets differ from each other. The ultrathin nanosheets give much broader and less intense peaks. The full width at half-maximum (FWHM) of the (001) peak of the obtained Bi$_{0.9}$Eu$_{0.1}$OCl ultrathin nanosheet and nanoplate are 1.74° and 0.41°, respectively. The XRD patterns of Bi$_{0.9}$Eu$_{0.1}$OCl nanoplates consist of sharp and distinct diffraction peaks, indicating a higher crystalline nature and large grain size. Compared with Bi$_{0.9}$Eu$_{0.1}$OCl nanoplate, the diffraction intensity ratio of (110)/(001) planes for Bi$_{0.9}$Eu$_{0.1}$OCl ultrathin nanosheet is much higher, which is attributed to the ultrathin nanosheet oriented along the [001] orientation, with a relatively large lateral size oriented along the [110] direction.[30] The tetragonal structure of BiOCl:Eu^{3+} is evidence of the basic unit cell crystal structure (Fig. 1a). Fig. 1b and c show the XRD patterns of BiOCl nanosheets and nanoplates doped with different concentrations of Eu^{3+} ions. The XRD patterns do not show any significant changes with the increase in concentration of Eu^{3+} ions. The incorporation of Eu^{3+} ions into the host material can be verified from estimation of the unit cell parameters of the samples. Fig. 1d shows the relationship between the unit cell volumes and Eu^{3+} doping concentrations for both nanoplate and ultrathin nanosheet. The unit cell volume of Bi$_{1-x}$Eu$_x$OCl ultrathin nanosheets ($x = 0.01, 0.05, 0.07, 0.10$ and 0.13) is smaller than that of Bi$_{1-x}$Eu$_x$OCl nanoplates, which is consistent with the XRD results. The unit cell volumes were found to linearly decrease by about 0.16 and 0.17% for nanosheet and nanoplate samples, respectively, with an increase of Eu^{3+} in BiOCl, as the ionic radii of Eu^{3+} ($r = 1.066$ Å, CN = 8) is smaller than that of Bi^{3+} ($r = 1.17$ Å, CN = 8).[31] As a consequence, when Bi^{3+} is substituted by Eu^{3+}, the shrinkage of the unit cell volume is clearly observed, as expected.[32]

3.2 Morphology of BiOCl nanostructures

Fig. 2 shows the morphology of the as-prepared Bi$_{0.9}$Eu$_{0.1}$OCl nanostructures, as investigated by SEM and TEM images. The SEM image of Fig. 2a clearly shows the formation of nanoplates in the sample. The nanoplate size is in the range of 100–200 nm, with an estimated thickness of 15–20 nm. Fig. 2b shows the TEM imagery of the samples, and the formed particles are almost of square shape. The inset of Fig. 2b shows high magnification TEM imagery of a few square-like nanoplates. Fig. 2c shows the high crystallinity of the particles demonstrated by HRTEM imagery. This figure shows the formation of clear lattice fringes, and the d-spacing calculated from the lattice fringes is found to be 0.275 nm, which is in good agreement with the standard JCPDS card values. The clear 2D lattice fringe demonstrates the high crystallinity and smooth exposed facets of such large nanoplates. Fig. 2d shows the SEM imagery of Bi$_{0.9}$Eu$_{0.1}$OCl ultrathin nanosheet, which contains numerous square-like nanosheets having a size in the range of
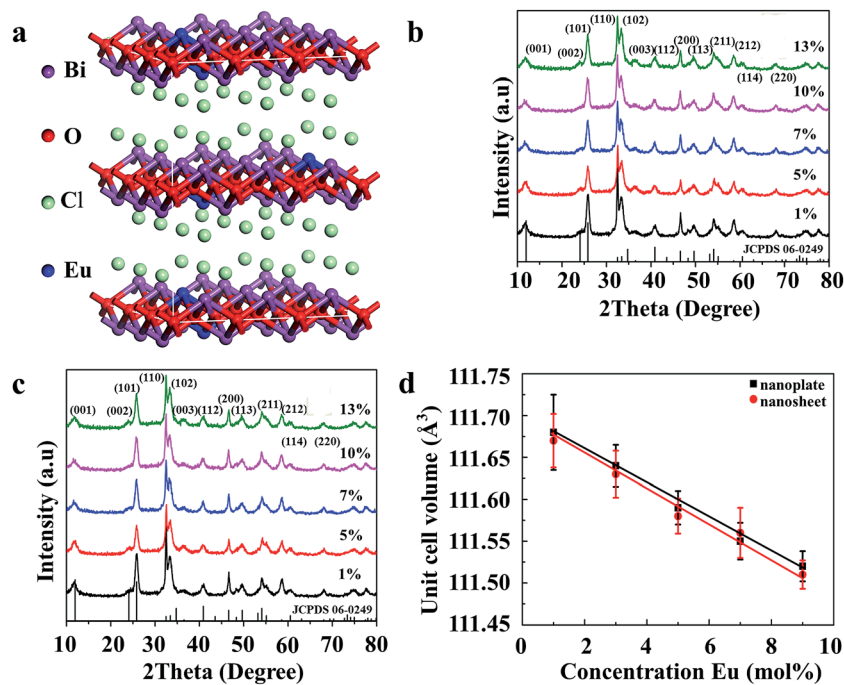
Fig. 1 (a) The structure of the BiOCl supercell. The purple, red, green and blue balls are Bi, O, Cl and Eu, respectively. The XRD patterns of (b) nanosheet, and (c) nanoplate of $Bi_{1-x}Eu_xOCl$ samples. (d) The concentration dependence of unit cell volume for nanosheet and nanoplate of $Bi_{1-x}Eu_xOCl$ samples ($x = 0.01$, 0.05, 0.07, 0.10 and 0.13).

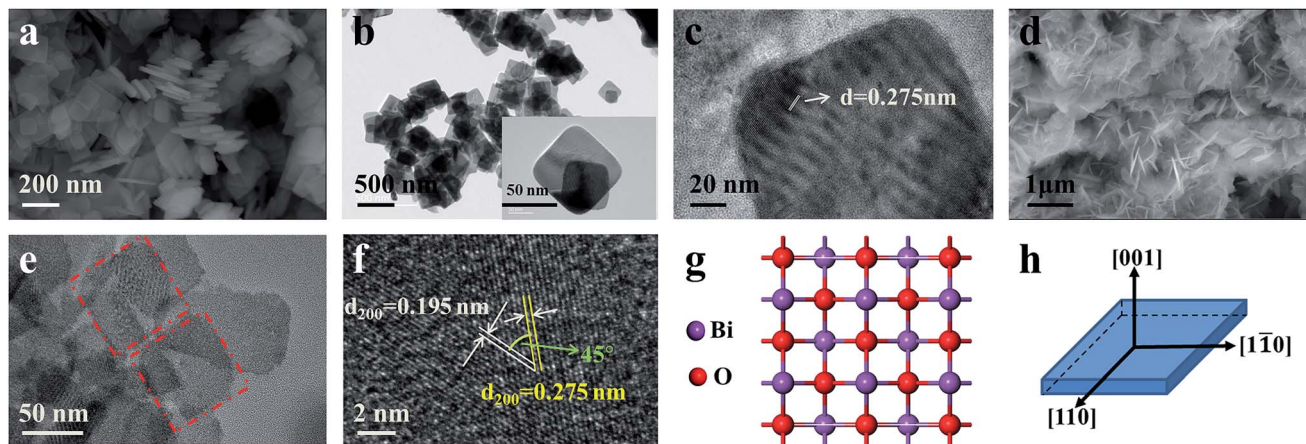**Fig. 2** (a) SEM, (b) TEM, and (c) HRTEM of $Bi_{0.9}Eu_{0.1}OCl$ nanoplate. (d) SEM, (e) TEM, and (f) HRTEM of $Bi_{0.9}Eu_{0.1}OCl$ ultrathin nanosheet. (g) View of the structure of the {001} facet, and (h) schematic illustration of the crystal orientation.

50–100 nm. During the synthesis process, we found that the existence of PVP exhibits a significant influence on the formation of $BiOCl:Eu^{3+}$ ultrathin nanosheets. It is well known that the commonly used PVP is an effective surfactant, which can function as a surface stabilizer, and its long polymeric chain structure will completely surround one or more nuclear Bi oxyhalides.[33] Importantly, the PVP can be adsorbed on the specific plane, and controls the growth of 2D nanostructures of BiOCl.[34,35] Fig. 2e shows the TEM imagery that contains numerous square-like nanosheets having a size in the range of 50–100 nm. The HRTEM image (Fig. 2f) exhibits continuous lattice fringes with an interplanar lattice spacing of 0.275 nm.

The angle of adjacent spots labeled in the HRTEM pattern is 45°, which is identical to the theoretical value of the angle between the (110) and (200) planes of tetragonal BiOCl. Fig. 2g shows the BiOCl [001] crystal structure, and reveals Bi and O atoms in a specific crystal plane. On the basis of the above structural and morphology information, the crystal orientation is as shown in Fig. 2h, where the top and bottom surfaces of the nanosheet are {001} facets, while the four lateral surfaces are {110} facets.[36] The $Bi_{0.9}Eu_{0.1}OCl$ nanoplate was also prepared for comparison under similar conditions as the $Bi_{0.9}Eu_{0.1}OCl$ ultrathin nanosheet. Presuming that the length of each $Bi_{0.9}$-$Eu_{0.1}OCl$ nanostructure sample was the same as its width, the

percentage of the {001} facets was estimated to be 86 and 36% for $Bi_{0.9}Eu_{0.1}OCl$ ultrathin nanosheet and nanoplate, respectively. It is widely accepted that the {001} facets of BiOCl possess a high oxygen density,[37] and the surface energy of O-terminated (001) surfaces was much smaller than the surface energy of Bi-terminated (001) surfaces, which is co-governed by the surface atom exposure, and the site-generated oxygen vacancy of the (001) surface.[38] Consequently, the $Bi_{0.9}Eu_{0.1}OCl$ ultrathin nanosheets with exposed {001} facets are expected to exhibit more oxygen defects, when compared with the $Bi_{0.9}Eu_{0.1}OCl$ nanoplate.[39] Fig. 3b shows a cross-sectional line profile of the BiOCl ultrathin nanosheet (as marked in Fig. 3a), indicating that the thickness estimated to be 2.9 nm corresponds to 4 [Cl–Bi–O–Bi–Cl] layers. The lateral size of $Bi_{0.9}Eu_{0.1}OCl$ ultrathin nanosheet obtained by AFM is consistent with that from the TEM imagery, as shown in Fig. 3a.

3.3 Identification of oxygen vacancy of Eu³⁺ activated BiOCl ultrathin nanosheets

Fig. 4a shows that XPS analysis to identify the defects in the $Bi_{0.9}Eu_{0.1}OCl$ ultrathin nanosheet and nanoplate. Fig. 4b shows the high-resolution Bi 4f XPS spectra of $Bi_{0.9}Eu_{0.1}OCl$ ultrathin nanosheets and nanoplates. Compared with $Bi_{0.9}Eu_{0.1}OCl$

nanoplates, the Bi 4f peaks of $Bi_{0.9}Eu_{0.1}OCl$ ultrathin nanosheets shift to a higher binding energy. Furthermore, the binding energy of O 1s is about 529.05 eV for $Bi_{0.9}Eu_{0.1}OCl$ ultrathin nanosheets, which is smaller than the 530.8 eV of $Bi_{0.9}Eu_{0.1}OCl$ nanoplates (Fig. 4c). This shift may be attributed to the weakened hybridization between Bi 6s and O 2p, which leads to the decrease of binding energy of bismuth–oxygen bond (Bi–O).[40] These shifts indicate the formation of surface oxygen vacancies in the $Bi_{0.9}Eu_{0.1}OCl$ ultrathin nanosheets.[41]

3.4 Luminescence of Eu³⁺ activated BiOCl ultrathin nanosheets and BiOCl nanoplates

Zhao *et al.* analyzed the band gap of BiOCl:Eu³⁺ crystals through first-principles calculations, and confirmed the possibility of forming impurity levels due to Eu³⁺ doping.[24,25] In this work, the DFT calculations have been applied to investigate the impurity level changes of the ultrathin $Bi_{0.9}Eu_{0.1}OCl$ nanosheet. Fig. S2 and S3† show the crystal structure models, while Fig. S4 and S5† show the band structures of pure BiOCl and $Bi_{0.9}Eu_{0.1}OCl$. The impurity levels lead to the energy transfer from BiOCl to Eu³⁺ 4f state. The number of impurity levels increase with the increase of Eu³⁺ concentration, and finally show metallic property.[42,43] To evaluate the effect of oxygen vacancy on the energy gap of the
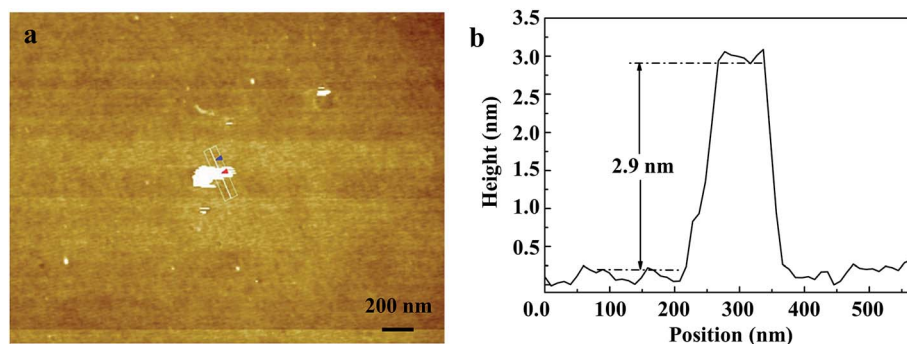

Fig. 3 (a) AFM image of $Bi_{0.9}Eu_{0.1}OCl$ ultrathin nanosheet. (b) Cross-section line profile of the $Bi_{0.9}Eu_{0.1}OCl$ ultrathin nanosheet shown in (a).
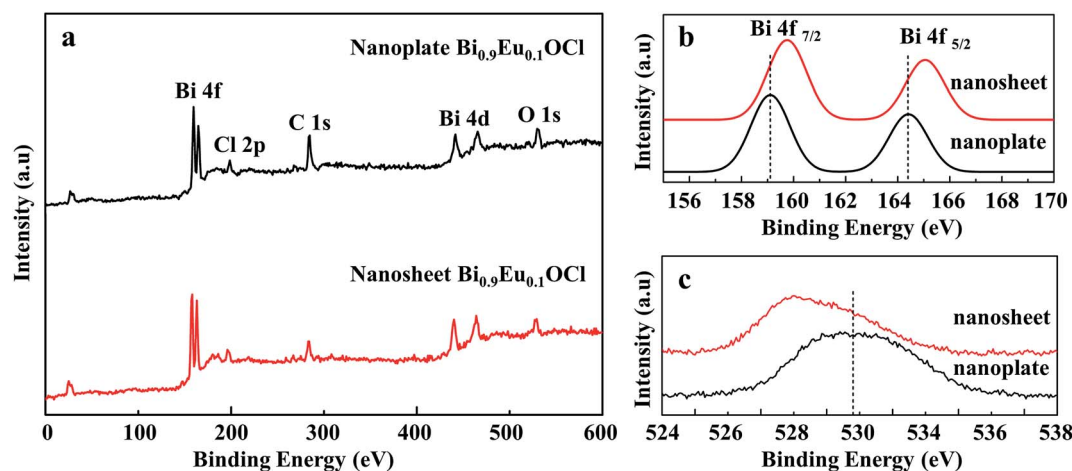

Fig. 4 (a) Survey XPS spectrum and high-resolution XPS spectra of $Bi_{0.9}Eu_{0.1}OCl$ ultrathin nanosheet and nanoplate, (b) Bi 4f, and (c) the O 1s region for $Bi_{0.9}Eu_{0.1}OCl$ ultrathin nanosheet and nanoplate.

BiOCl:Eu³⁺ nanoplate and ultrathin nanosheets. Fig. S6 and S7 of the ESI† show the UV-Vis absorption spectra BiOCl with different Eu³⁺ concentrations. The band gap values calculated based on the Kubelka–Munk theory are shown in the insets of Fig. S6 and S7.† The band gap for the ultrathin nanosheets were found to be 3.2–3.35 eV, smaller than that of the nanoplates (3.36–3.4 eV). This is due to the fact that the oxygen vacancies play a role of narrowing the band gap instead of forming the impurity levels.[44] The band gap becomes narrower with the increase in Eu³⁺ concentration for BiOCl ultrathin nanosheets and nanoplates (insets of Fig. S6 and S7†). This phenomenon is known as band gap narrowing (BGN), which is consistent with DFT calculations, as shown in Fig. S4 and S5,† the impurity states become more delocalized and overlap with the VB edge and raise the position of the VB. As a consequence, the raised VB band is beneficial for separation of the photo-induced electron–hole pairs.[45] In the case of luminescence, there are more photogenerated electrons or holes that could transfer to Eu³⁺, resulting in enhancement of the emission intensity as expected.

Fig. 5a shows the excitation spectra of ultrathin nanosheets and nanoplates of Bi₀.₉Eu₀.₁OCl monitored at 616 nm (⁵D₀ → ⁷F₂ transition) emission wavelength. The spectra reveal a broadband in the wavelength range of 300–450 nm, with the peak at 380 nm. The broadband is due to the transition from valence band to conduction band in the BiOCl host lattice.[27] The intensity of broad band is higher for the ultrathin nanosheets than for the nanoplates. The intra-configurational f–f transitions of Eu³⁺ overlap with the host broadband, and are observed as weak peaks. The f–f transitions from ⁷F₀ to ⁵G₂, ⁵G₃, ⁵L₆ and ⁵D₃ electronic transitions are observed at 377, 382, 394 and 416 nm, respectively. The peak at 464 nm is attributed to the ⁷F₀ → ⁵D₂ electronic transition. These peaks are clearly observed for the nanoplate sample, as the intensity of the host absorption band is weak. The results indicate that the BiOCl:Eu³⁺ phosphor own excellent broadband NUV-exciting ability. Fig. 5b shows the recorded emission spectra of f–f ultrathin nanosheets and nanoplates upon 380 nm excitation. The emission spectra show several sharp and well-resolved emission lines of Eu³⁺ corresponding to the radiative relaxations from the excited state (⁵D₀)

level to its low-lying multiplets ^7F_J ($J = 0, 1, 2, 3, 4$). The strongest emission centered at around 616 nm corresponds to the electrical dipole transition ($^5D_0 \rightarrow {}^7F_2$) of Eu³⁺, indicating that the Eu³⁺ ions occupy the sites without inversion symmetry. Other line emission lines at about 578, 592, 650 and 697 nm are associated with $^5D_0 \rightarrow {}^7F_0$, $^7F_1$ (magnetic dipole transition), $^7F_3$, and $^7F_4$ transitions of Eu³⁺, respectively. The ultrathin nanosheet shows stronger emission intensity than the nanoplates sample. The inset of Fig. 5b shows that as the Eu³⁺ concentration increases from 1 to 10 mol%, the emission intensity increases. Furthermore, as the Eu concentration reaches 10 mol%, the emission intensity decreases, due to the concentration quenching effect. When the Eu³⁺ ions concentration increases, the distance between Eu and Eu decreases, which results in the increase of nonradiative energy transfer between the dopant ions. The distance at which the nonradiative transfer become comparable with the radiative emission is known as the critical distance (R_c). The R_c value can be estimated by the following well-known Blasse's equation:[46]

$$R_c \approx 2(3V/4\pi X_c N)^{1/3}$$

where, X_c is the critical concentration, N is the number of cationic sites in the unit cell, and V is the volume of the unit cell. The calculated R_c value was estimated to be 10.21 Å at 10 mol% of Eu³⁺ concentration. Here, R_c is larger than 5 Å, which indicates that the major mechanism for concentration quenching of BiOCl:Eu³⁺ phosphors is multipolar interaction.[47] Dexter and Schulman proposed a theory to determine the exact type of interaction involved in the energy transfer. Dexter's formula for multipolar interaction and Reisfeld's approximation are as follows:[48]

$$I/C = K_1/\beta C^{s/3}$$

where, C is the activator concentration involved in self concentration quenching, and K_1 and β are constants for each interaction in the same excitation conditions for a given host lattice. The s values of 3, 6, 8, and 10 indicate the exchange coupling, dipole–dipole (d–d), dipole–quadrupole (d–q), and
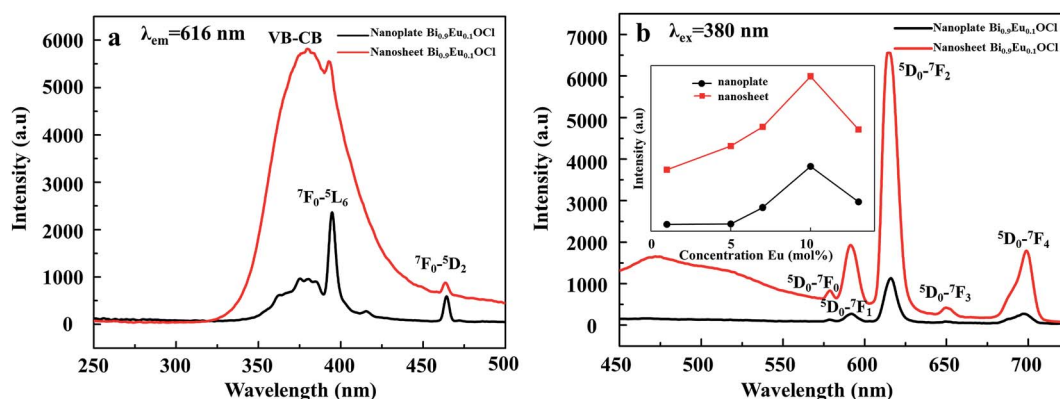

Fig. 5 (a) Excitation spectra of Bi₀.₉Eu₀.₁OCl ultrathin nanosheet and nanoplate (the inset is the luminescence intensity dependence of the Eu³⁺ concentrations). (b) Emission spectra of Bi₀.₉Eu₀.₁OCl ultrathin nanosheet and nanoplate.
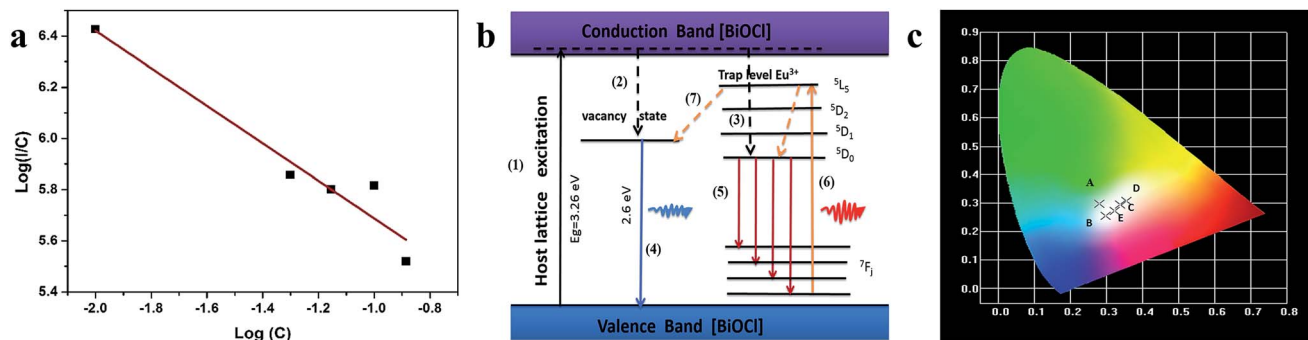
Fig. 6 (a) log plot for the emission intensity per Eu^{3+} ions as a function of Eu^{3+} concentration. (b) A possible mechanism of luminescence of BiOCl:Eu^{3+} ultrathin nanosheets. (c) The CIE chromaticity diagram of $Bi_{1-x}Eu_xOCl$ ultrathin nanosheets; the five points are as follows: (A) $Bi_{0.99}Eu_{0.01}OCl$, (B) $Bi_{0.95}Eu_{0.5}OCl$, (C) $Bi_{0.93}Eu_{0.7}OCl$, (D) $Bi_{0.9}Eu_{0.1}OCl$, and (E) $Bi_{0.87}Eu_{0.13}OCl$ ultrathin nanosheet, upon excitation at 380 nm.

quadrupole–quadrupole (q–q) interactions, respectively. The value of s can be determined from the slope ($s/3$) of the linear fit obtained from the plots of $\log(I/C)$ *versus* $\log C$ (Fig. 6a). The slope of the linear fit was found to be 0.73, and the s value was found to be 2.19 (close to the theoretical value of 3 for the exchange coupling). This indicates that exchange coupling is the major mechanism for the concentration quenching in BiOCl:Eu^{3+} phosphors.

An observation of note is the broad emission band centered at around 475 nm with a small shoulder, which probably originates from the oxygen vacancies. Such weak emission can arise in BiOCl:Eu^{3+} due to the transition of an electron from the conduction band (CB) to the valance band (VB) *via* oxygen vacancy state and trap levels. Under 380 nm excitation, Eu^{3+} emission can be observed, indicating efficient energy transfer from Eu^{3+} to oxygen vacancy. Because the Eu^{3+} concentrations in the different final products are the same, the different luminescence behaviors can be ascribed to the different morphologies of the two samples. Fig. 5b shows that the relative intensities of the PL peaks of the nanoplate exhibit weak luminescence. However, a significant enhancement of up to 600% was observed in the red luminescence intensity for the BiOCl:Eu^{3+} ultrathin nanosheets, compared with the nanoplates. The nanosheets of only 2.9 nm in thickness show more surface defects than the nanoplates. These results indicate that the luminescence properties of BiOCl:Eu^{3+} are very sensitive to its morphology, and are strongly dependent on the surface defects, *i.e.* more oxygen vacancies from the ultrathin nanosheet may also result in a strong emission intensity. BiOCl:Eu^{3+} ultrathin nanosheet has a large number of oxygen vacancies, as has been demonstrated by the XPS result. The origin of PL spectra includes red emission from Eu^{3+}, and blue emission from the oxygen vacancy. As the thickness of BiOCl:Eu^{3+} decreases, the concentration of oxygen vacancies increases as the luminescence centres. This is the reason for the increasing emission intensity with decreasing thickness of BiOCl:Eu^{3+}.

The PL mechanisms of BiOCl ultrathin nanosheet are mainly attributed to the effect of oxygen vacancies, which inevitably occur during the crystallization process. The oxygen vacancy acts as an electron trap to capture the electron.[49] Fig. 6b shows a possible mechanism of the luminescence of BiOCl:Eu^{3+} ultrathin nanosheets. Under the excitation of UV light, the electrons coupled with excitation energy can be promoted from valence band to conduction band (progression (1)). In the conduction band, most of the electrons are then relaxed to the oxygen vacant state and luminescence centers of Eu^{3+} states *via* the non-radiative transitions (progressions (2, 3)), followed by the radiative transition to ground states. The broad peak below 550 nm is due to process (4), and the characteristic emission of Eu^{3+} is due to progression (5). With the 394 nm excitation, the energy transferring from the Eu^{3+} to oxygen vacancy (progression (6)) was observed, along with the Eu^{3+} emission. At the same time, the same progressions (4) & (5) occurred, and resulting in characteristic emission of Eu^{3+}. Then, the intensity of red luminescence was observed.

Fig. 6c shows the commission international de l'éclairage (CIE) chromaticity coordinates of BiOCl:Eu^{3+} ultrathin nanosheets excited at 380 nm. This figure shows that the CIE chromaticity coordinates of $Bi_{0.99}Eu_{0.01}OCl$ (0.281, 0.298) are around the blue-green, $Bi_{0.95}Eu_{0.05}OCl$ (0.297, 0.255), $Bi_{0.87}Eu_{0.13}OCl$ (0.322, 0.271), and $Bi_{0.93}Eu_{0.07}OCl$ (0.338, 0.295) are around the white, and $Bi_{0.9}Eu_{0.1}OCl$ (0.355, 0.308) are around the orange-yellow regions, indicating that the emission color can be tuned by modulation of the Eu^{3+} ion concentration from blue-green to white, and finally to yellow. The results suggest that the CIE chromaticity coordinates are tunable with the change in Eu^{3+} ions concentration.

4. Conclusions

Color tunable white-light emitting BiOCl:Eu^{3+} nanosheets were successfully synthesized with a facile solvothermal method. BiOCl:Eu^{3+} nanoparticles were also successfully synthesized by a facile solvothermal method. The thickness and size of the nanoparticles were controlled with PVP. Nanosheets of size around 50–100 nm and thickness of 2.9 nm were formed in the presence of PVP, and nanoplates were formed in its absence. The band gap of the materials also decreased, due to the decrease in the thinness of the particles, and it also further decreased with the Eu^{3+} ions doping. The BiOCl:Eu^{3+} ultrathin nanosheets phosphor sample showed higher intensity than the nanoplates sample, due to the formation of oxygen vacancies.

The nanosheets sample showed white-light emission, due to the combined emission from the host and the dopant ions. Importantly, these $BiOCl:Eu^{3+}$ ultrathin nanosheets phosphors showed color-tunable emissions, due to the energy transfer from the BiOCl host to Eu^{3+} ions and the oxygen vacancies. The tunable color-emitting ultrathin $BiOCl:Eu^{3+}$ phosphors exhibit potential as a kind of phosphor-converted materials for NUV white LEDs.

Acknowledgements

Notes and references

1 B. Radisavljevic, A. Radenovic, J. Brivio, V. Giacometti and A. Kis, *Nat. Nanotechnol.*, 2011, **6**, 147–150.

2 Y. W. Zhu, S. T. Murali, M. D. Stoller, K. J. Ganesh, W. W. Cai, P. J. Ferreira and A. Pirkle, *Science*, 2011, **332**, 1537–1541.

3 K. S. Novoselov, A. K. Geim, S. V. Morozov, D. Jiang, Y. Zhang, S. V. Dubonos, I. V. Grigorieva and A. A. Firsov, *Science*, 2004, **306**, 666–669.

4 K. S. Novoselov, D. Jiang, F. Schedin, T. J. Booth, V. V. Khotkevich, S. V. Morozov and A. K. Geim, *Proc. Natl. Acad. Sci. U. S. A.*, 2005, **102**, 10451–10453.

5 S. Bae, H. Kim, Y. Lee, X. Xu, J. S. Park and Y. Zhang, *Nat. Nanotechnol.*, 2010, **5**, 574–578.

6 A. Pospischil, M. M. Furchi and T. Mueller, *Nat. Nanotechnol.*, 2014, **9**, 257–261.

7 X. Zang, Q. Chen, P. Li, Y. He, X. Li and M. Zhu, *Small*, 2014, **10**, 2583–2588.

8 R. Ganatra and Q. Zhang, *ACS Nano*, 2014, **8**, 4074–4099.

9 X. Li, X. Zang, X. Li, M. Zhu, Q. Chen, K. L. Wang, M. L. Zhong, J. Q. Wei, D. H. Wu and H. W. Zhu, *Adv. Energy Mater.*, 2014, **4**, 1400224.

10 K. F. Mak, C. G. Lee, J. Hone, J. Shan and T. F. Heinz, *Phys. Rev. Lett.*, 2010, **105**, 136805.

11 C. O. Tadashi, F. Katsutoshi, A. Kosho, E. Yasuo, S. Takayoshi, K. Keiji and K. Kosuke, *J. Phys. Chem. C*, 2008, **112**, 17115–17120.

12 C. O. Tadashi, F. Katsutoshi, A. Kosho, E. Yasuo and S. Takayoshi, *Chem. Mater.*, 2007, **19**, 6575–6580.

13 G. L. Frey, K. J. Reynolds and R. H. Friend, *Adv. Mater.*, 2002, **14**, 265–268.

14 S. J. Wu, C. Wang, Y. F. Cui, T. M. Wang, B. B. Huang, X. X. Zhang and X. Y. Qin, *Mater. Lett.*, 2010, **64**, 115–118.

15 G. G. Briand and N. Burford, *Chem. Rev.*, 1999, **99**, 2601–2658.

16 N. Kijima, K. Matano, M. Saito, T. Oikawa, T. Konishi, H. Yasuda, T. Sato and Y. Yoshimura, *Appl. Catal., A*, 2001, **206**, 237–244.

17 X. Zhang, Z. Ai, F. Jia and L. Zhang, *J. Phys. Chem. C*, 2008, **112**, 747–753.

18 Z. Deng, D. Chen, B. Peng and F. Tang, *Cryst. Growth Des.*, 2008, **8**, 2995–3003.

19 K. Zhang, J. Liang, S. Wang, J. Liu, K. Ren, X. Zheng, H. Luo, Y. Peng, X. Zou, X. Bo, J. Li and X. Yu, *Cryst. Growth Des.*, 2011, **12**, 793–803.

20 L. Chen, R. Huang, M. Xiong, Q. Yuan, J. He, J. Jia, M. Y. Yao, S. L. Luo, C. Au and S. F. Yin, *Inorg. Chem.*, 2013, **52**, 11118–11125.

21 Y. Lei, G. Wang, S. S. Fan and W. Zhang, *CrystEngComm*, 2009, **11**, 1857–1862.

22 H. Yamashita and H. X. Li, *Nanostructured Photocatalysts: Adv. Funct. Mater.*, 2016, vol. 333.

23 Y. J. Li, Z. Y. Zhao, Z. G. Song, R. H. Wan, J. B. Qiu and Z. W. Yang, *J. Am. Ceram. Soc.*, 2015, **98**, 2170–2176.

24 D. Peng and S. Y. Jae, *Mater. Lett.*, 2016, **169**, 135–139.

25 D. Armita, S. Shyam, N. K. B. V. Adusumalli and V. Mahalingam, *Langmuir*, 2014, **30**, 1401–1409.

26 Y. Y. Guo, Z. J. Zhang, G. Q. Zhu and W. Yang, *Appl. Surf. Sci.*, 2016, **388**, 345–351.

27 M. L. Guan, C. Xiao, J. Zhang, S. J. Fan, R. An, Q. M. Cheng and Y. Xie, *J. Am. Chem. Soc.*, 2013, **135**, 10411–10417.

28 J. Yi and Z. Y. Zhao, *J. Lumin.*, 2014, **156**, 205–211.

29 Z. Y. Zhao and W. W. Dai, *Inorg. Chem.*, 2014, **53**, 13001–13011.

30 L. Q. Ye, X. L. Jin, Y. M. Leng, Y. R. Su, H. Q. Xie and C. Liu, *J. Power Sources*, 2015, **293**, 409–415.

31 R. D. Shannon, *Acta Crystallogr., Sect. A: Cryst. Phys., Diffr., Theor. Gen. Crystallogr.*, 1976, **32**, 751–767.

32 I. V. B. Maggay, P. C. Lin and W. R. Liu, *J. Solid State Light.*, 2014, **1**, 13–27.

33 Z. T. Deng, F. Q. Tang, D. Chen, X. W. Meng, L. Cao and B. S. Zou, *J. Phys. Chem. B*, 2006, **110**, 18225–18230.

34 Z. T. Deng, D. Chen, B. Peng and F. Q. Tang, *Cryst. Growth Des.*, 2008, **8**, 2995–3003.

35 M. Li, R. M. Wang, J. Y. Zhang, H. Gao, F. Li, S. J. Lindquist and N. Q. Wu, *ACS Appl. Mater. Interfaces*, 2016, **8**, 6662–6668.

36 J. R. Jin, Y. J. Wang and T. He, *RSC Adv.*, 2015, **5**, 100244–100250.

37 L. Ye, L. Zan, L. Tian, T. Peng and J. Zhang, *Chem. Commun.*, 2011, **47**, 6951–6953.

38 K. Zhao, L. J. Zhang, Q. L. Wang, W. He and J. J. Yin, *J. Am. Chem. Soc.*, 2013, **135**, 15750–15753.

39 Y. H. Wu, B. Yuan, M. R. Li, W. H. Zhang, Y. Liu and C. Li, *Chem. Sci.*, 2015, **6**, 1873–1878.

40 J. Wang, W. J. Jiang, D. Liu, Z. Wei and Y. F. Zhu, *Appl. Catal., B*, 2015, **306**, 176–177.

41 J. Xu, Y. R. Teng and F. Teng, *Sci. Rep.*, 2016, **6**, 32457.

42 A. A. Dakhel, *J. Mater. Sci.*, 2011, **46**, 1455–1461.

43 M. Y. Guo, A. M. C. Ng, F. Z. Liu, A. B. Djurisic, W. K. Chan, H. M. Su and K. S. Wong, *J. Phys. Chem. C*, 2011, **115**, 11095–11101.

44 J. P. Wang, Z. Y. Wang, B. B. Huang, Y. D. Ma, Y. Y. Liu, X. Y. Qin, X. Y. Zhang and Y. Dai, *ACS Appl. Mater. Interfaces*, 2012, **4**, 4024–4030.

45 K. G. Santosh, P. S. Ghosh, M. Sahu, K. Bhattacharyya, R. Tewari and V. Natarajan, *RSC Adv.*, 2015, **5**, 58832–58842.

46 G. Blasse, *Phys. Lett. A*, 1968, **28**, 444–453.

47 Z. G. Xia, R. S. Liu, K. W. Huang and V. Drozd, *J. Mater. Chem.*, 2012, **22**, 15183–15189.

48 D. L. Dexter, *J. Chem. Phys.*, 1953, **21**, 836–850.

49 T. Aitasalo, P. Deren, J. Holsa, H. Jungner, J. C. Krupa, M. I. Lastusaar, J. Legendziewicz and J. W. Niittykoski, *J. Solid State Chem.*, 2003, **171**, 114–122.